

Discrete-Fresnel Domain Channel Estimation in OCDM-based Radar Systems

Lucas Giroto de Oliveira, *Graduate Student Member, IEEE*, Benjamin Nuss, *Graduate Student Member, IEEE*, Mohamad Basim Alabd, *Graduate Student Member, IEEE*, Axel Diewald, *Graduate Student Member, IEEE*, Yueheng Li, *Graduate Student Member, IEEE*, Linda Gehre, Xueyun Long, Theresa Antes, Johannes Galinsky, and Thomas Zwick, *Fellow, IEEE*

Abstract—In recent years, orthogonal chirp-division multiplexing (OCDM) has been increasingly considered as an alternative multicarrier scheme, e.g., to orthogonal frequency-division multiplexing, in digital communication applications. Among reasons for that are its demonstrated superior performance resulting from its robustness to impairments such as frequency selectivity of channels and intersymbol interference. Furthermore, the so-called unbiased channel estimation in the discrete-Fresnel domain has also been investigated for both communication and sensing systems, however without considering the effects of frequency shifts. This article investigates the suitability of the aforementioned discrete-Fresnel domain channel estimation in OCDM-based radar systems as an alternative to the correlation-based processing previously adopted, e.g., in the radar-communication (RadCom) literature, which yields high sidelobe level depending on the symbols modulated onto the orthogonal subchirps. In this context, a mathematical formulation for the aforementioned channel estimation approach is introduced. Additionally, extensions to multi-user/multiple-input multiple-output and RadCom operations are proposed. Finally, the performance of the proposed schemes is analyzed, and the presented discussion is supported by simulation and measurement results. In summary, all proposed OCDM-based schemes yield comparable radar sensing performance to their orthogonal frequency-division multiplexing counterpart, while achieving improved peak-to-average power ratio and, in the RadCom case, communication performance.

Index Terms—Channel estimation, multiple-input multiple-output (MIMO), orthogonal chirp-division multiplexing (OCDM), radar-communication (RadCom), radar sensing.

I. INTRODUCTION

ALL-digital radar systems have been increasingly gaining attention in recent years. While they impose the challenge of handling high data rates resulting from the use of digital-to-analog converters (DACs) and analog-to-digital converters (ADCs) with high resolutions and sampling rates [1], their use enables a wide range of possibilities. Among these are enabling efficient multi-user (MU) or multiple-input multiple-output (MIMO) operation, e.g., for distributed radar sensing or direction of arrival (DoA) estimation [2], while also yielding high unambiguous velocity and fine range resolution.

Manuscript received MM DD, 2022. The authors acknowledge the financial support by the Federal Ministry of Education and Research of Germany in the project “Open6GHub” (grant number: 16KISK010). The work of Lucas Giroto de Oliveira was also financed by the German Academic Exchange Service (DAAD) - Funding program 57440921/Pers. Ref. No. 91555731. (Corresponding author: Lucas Giroto de Oliveira.)

The authors are with the Institute of Radio Frequency Engineering and Electronics (IHE), Karlsruhe Institute of Technology (KIT), 76131 Karlsruhe, Germany (e-mail: lucas.oliveira@kit.edu).

Further aspects of all-digital radar systems also include higher signal processing flexibility and improved performance for joint radar-communication (RadCom) operation [3].

The possibilities enabled by all-digital radar systems rely on the use of efficient modulation schemes, among which are the widely-known orthogonal frequency-division multiplexing (OFDM), phase-modulated continuous wave (PMCW) [4]–[8], and orthogonal chirp-division multiplexing (OCDM) [9]. The latter has been recently investigated in an integrated sensing and communication (ISAC) context [10], [11] to enable joint RadCom operation [12], [13] or applications such as joint sonar-communication [14]. On the one hand, OCDM is known to outperform its aforementioned counterparts for communication purposes [3], [15], e.g., due to its multicarrier and spread spectrum characteristics [16], [17] that yield robustness to multipath propagation, Doppler shifts, intersymbol interference (ISI) [18], and narrowband interference (NBI) [19]. On the other hand, the radar sensing performance of conventional OCDM-based systems is limited. Examples include the relatively high range sidelobe level that is influenced by modulated symbols onto the orthogonal subchirps in the OCDM-based RadCom systems with correlation-based radar signal processing [3], [12], [13], [20].

In the face of limitations of typical radar processing schemes for OCDM-based systems, a potential alternative is the use of discrete-Fresnel domain channel estimation, which has been introduced in [21] for coherent optical OFDM systems and further investigated in [22] and [23]. The aforementioned channel estimation strategy has also been used in the context of sensing, namely for enabling reflectometric sensing of power lines [24] with a baseband OCDM system [25]. The simplest discrete-Fresnel domain channel estimation strategy consists of transmitting a pilot OCDM symbol where only the first subchirp is active. Based on the convolution theorem of the discrete Fresnel transform (DFnT) [16], the receive OCDM symbol will ultimately contain a channel impulse response (CIR) estimate. The aforementioned studies have, however, considered that the estimated channel only introduces delays in the transmit signal. Frequency shifts were either not considered [21], [22] or assumed to be compensated [23]. While the assumption that frequency shifts are compensated may be reasonable for communication purposes, where, e.g., Schmidl & Cox’s algorithm [26], [27] can be used, it does not necessarily hold for radar systems. Although transmit and receive channels usually share the same oscillator and are

fully synchronized, Doppler shifts introduced by the motion of targets are not compensated during radar channel estimation. In fact, the goal of radar sensing is jointly estimating the range and Doppler shift, and consequently relative radial velocity, of targets. The lack of compensation for Doppler shifts, which are essentially frequency shifts, results in the need for a more thorough investigation of the discrete-Fresnel domain channel estimation for OCDM-based radar systems, which is the subject of this article.

The main contributions of this article are as follows:

- A thorough mathematical formulation of the effects of time and frequency shifts in the discrete-Fresnel domain, both applied individually or jointly. It is shown that both aforementioned effects cause shifts and phase rotations of subchirps in the discrete-Fresnel domain, leading to interchirp interference (IChI) and resembling the inter-carrier interference (ICI) in OFDM-based systems [28]. These findings extend the state-of-the-art knowledge on propagation effects on OCDM signals, which previously only consider the effects of time shifts described by the convolution theorem of the DF_nT, and can be used in the contexts of radar, communication, and RadCom systems.
- A detailed description of discrete-Fresnel domain radar channel estimation, with closed-form expressions to analyze results for multiple point targets with distinct ranges and relative radial velocities and radar performance parameters including processing gain, range resolution and ambiguity, and velocity resolution and ambiguity.
- An extension of the investigated discrete-Fresnel domain radar channel estimation to MU/MIMO and RadCom operation based on a strategic subchirp allocation known as Fresnel-division multiplexing (FrDM), with remarks on eventually changed radar performance parameters.
- A performance analysis based on simulation and measurement results. The presented analysis covers an investigation of biases from ideally estimated CIRs under different Doppler shifts, which is supported by an analysis of signal-to-noise ratio (SNR) degradation and sidelobe level changes. Additionally, comparisons with the well-known OFDM RadCom are performed. The achieved results show that the proposed OCDM-based schemes present comparable radar sensing performance to OFDM, while presenting lower peak-to-average power ratio (PAPR) due to a similar effect to the known tone reservation in OFDM systems. Furthermore, the proposed extension of the proposed OCDM-based radar system to RadCom operation, which is named sector-modulated OCDM-based RadCom, yields improved communication robustness w.r.t. OFDM, as it retains the spread-spectrum characteristics of conventional OCDM schemes.

The remainder of this article is organized as follows. Section II presents a thorough mathematical description of the individual and joint effects of time and frequency shifts in the discrete-Fresnel domain. Based on these results, Section III mathematically formulates the discrete-Fresnel domain channel estimation for OCDM-based radar systems in detail and presents extensions of the introduced concept to MU/MIMO

and RadCom operations. Next, Section IV presents a performance analysis of the aforementioned schemes based on simulation and measurement results, and, finally, concluding remarks are given in Section V.

Notation

Throughout this article, t denotes time in seconds and f denotes frequency in Hertz. Additionally, $\delta[\chi]$, $\chi \in \mathbb{Z}$, is the Kronecker delta function, $\langle \cdot \rangle_v$ is the modulo v operator, $v \in \mathbb{N}_+$, and $\mathbb{E}\{\cdot\}$ is the expectation operator.

II. EFFECTS OF TIME AND FREQUENCY SHIFTS IN THE DISCRETE-FRESNEL DOMAIN

Let the matrix $\dot{\mathbf{X}} \in \mathbb{C}^{N \times M}$ be the discrete-Fresnel domain representation of the transmit frame in an OCDM-based system, with $N \in \mathbb{N}_+$ denoting both the OCDM symbol length and the number of subchirps in the OCDM system and $M \in \mathbb{N}_+$ denoting the total number of OCDM symbols in the frame. Before transmission over a channel, $\dot{\mathbf{X}}$ undergoes inverse discrete Fresnel transforms (IDF_nTs) along its columns to produce the discrete-time domain representation of the OCDM frame $\mathbf{x} \in \mathbb{C}^{N \times M}$ [3], [9], [12]. Consequently, the relationship between the element $x_{n,m} \in \mathbb{C}$ at the n th row, $n \in \{0, 1, \dots, N-1\}$, and m th column, $m \in \{0, 1, \dots, M-1\}$, of \mathbf{x} and the element $\dot{X}_{n,m} \in \mathbb{C}$ at the same position of $\dot{\mathbf{X}}$ is expressed as

$$x_{n,m} = \frac{1}{N} e^{j\frac{\pi}{4}} \sum_{k=0}^{N-1} \dot{X}_{k,m} e^{-j\frac{\pi}{N}(n-k)^2}, \quad (1)$$

where $k \in \{0, 1, \dots, N-1\}$ is the subchirp index for all of the M discrete-Fresnel domain representations of OCDM symbols contained in $\dot{\mathbf{X}}$. To prevent ISI, cyclic prefixes (CPs) of length N_{CP} are prepended to each of the M columns of \mathbf{x} , resulting in $\mathbf{x}_{\text{CP}} \in \mathbb{C}^{(N+N_{\text{CP}}) \times M}$. For successful ISI avoidance, it must hold that $N_{\text{CP}} \geq N_h - 1$, where N_h is the expected length of the discrete-time domain representation of the CIR. Next, \mathbf{x}_{CP} undergoes serial-to-parallel (S/P) conversion, and the real and imaginary parts of the resulting vector individually undergo digital-to-analog (D/A) conversion with sampling rate $F_s \geq B$, where B is the bandwidth occupied by the OCDM-based system in Hertz. The output signals by the two aforementioned DACs then undergo analog conditioning and I/Q modulation to a carrier with frequency $f_c \gg B$. Finally, the resulting continuous-time domain transmit signal $x(t) \in \mathbb{C}$, which occupies the radio-frequency (RF) band $f \in [f_c - B/2, f_c + B/2]$, is sent out by the transmit antenna of the OCDM-based system and propagates through a channel that has CIR $h(t) \in \mathbb{C}$ and may also introduce frequency shifts in its output signal.

At the receiver side of the OCDM-based system, the continuous-time domain output signal from the channel $y(t) \in \mathbb{C}$ is received by the receive antenna, undergoing down-conversion and analog conditioning in an I/Q receiver and finally analog-to-digital (A/D) conversion with sampling rate F_s . The samples from I and Q channels are then combined into the real and imaginary parts of a serial vector, which

after S/P conversion becomes the matrix $\mathbf{y}_{\text{CP}} \in \mathbb{C}^{(N+N_{\text{CP}}) \times M}$ that represents the discrete-time domain receive OCDM frame. In case $F_s > B$, it is also assumed that a prior downsampling to B is performed. An inverse processing to the one performed at the transmitter side is then performed on \mathbf{y}_{CP} , namely, CP removal to produce $\mathbf{y} \in \mathbb{C}^{N \times M}$, and column-wise DFNT, which ultimately produces the matrix $\dot{\mathbf{Y}} \in \mathbb{C}^{N \times M}$ that represents the discrete-Fresnel domain receive OCDM frame. The relationship between the element $\dot{Y}_{k,m} \in \mathbb{C}$ at the k th row and m th column of $\dot{\mathbf{Y}}$ and the element $y_{n,m} \in \mathbb{C}$ at the same position of \mathbf{y} is expressed as

$$\dot{Y}_{k,m} = e^{-j\frac{\pi}{4}} \sum_{n=0}^{N-1} y_{n,m} e^{j\frac{\pi}{N}(n-k)^2}. \quad (2)$$

For the sake of simplicity, additive white Gaussian noise (AWGN) is neither considered in (2) nor in the following expressions throughout this study since the DFNT operation does not change its statistics. This is supported by the claims in [9] and further discussion on this topic can be found in [15].

In systems such as wireless communication, radar, and RadCom systems, additional processing steps to the aforementioned ones are usually performed. In this section, however, the focus is on analyzing the effects of the propagation through a channel on the originally transmitted OCDM symbol representations contained in $\dot{\mathbf{X}}$, i.e., defining the relationship between $\dot{\mathbf{Y}}$ and $\dot{\mathbf{X}}$. The two main effects experienced due to the propagation through a channel are frequency and time shifts. The first are caused by the experienced circular convolution of each of the M columns of \mathbf{x} , which represent the discrete-time domain transmit OCDM symbols, with the discrete-time domain CIR representation $\mathbf{h} \in \mathbb{C}^{N_h \times 1} | \mathbf{h} = [h_0, h_1, \dots, h_{N_h-1}]^T$. In their turn, the latter effects encompass Doppler shifts caused by reflections off moving scatterers. In this context, Subsections II-A and II-B analyze the sole effects of frequency and time shifts in the discrete-Fresnel domain frame $\dot{\mathbf{Y}}$, respectively, while Subsection II-C addresses the case where time and frequency shifts are jointly experienced.

A. Effects of frequency shifts in the discrete-Fresnel domain

If a frequency shift f_Δ is the only experienced effect during propagation of the transmit OCDM signal through a channel, then the element at the n th row and m th column of the discrete-time domain frame \mathbf{y} obtained after CP removal at the receiver side can be expressed as

$$\begin{aligned} y_{n,m} &= x_{n,m} e^{j2\pi f_\Delta [m(N+N_{\text{CP}})+N_{\text{CP}}+n]/B} \\ &= x_{n,m} e^{j2\pi f_\Delta n/B} e^{j2\pi f_\Delta [m(N+N_{\text{CP}})+N_{\text{CP}}]/B}. \end{aligned} \quad (3)$$

For the sake of simplicity, the normalized frequency shift $k_\Delta \in \mathbb{R}$ and the phase $\phi_m \in \mathbb{R}$ are defined as

$$k_\Delta \triangleq f_\Delta / (B/N) \quad (4)$$

and

$$\phi_m \triangleq 2\pi k_\Delta [m(N+N_{\text{CP}})+N_{\text{CP}}]/N, \quad (5)$$

respectively. Next, performing column-wise DFNTs on \mathbf{y} yields the matrix $\dot{\mathbf{Y}}$, whose element at the k th row and m th column is expressed as

$$\begin{aligned} \dot{Y}_{k,m} &= e^{-j\frac{\pi}{4}} \sum_{n=0}^{N-1} \left(x_{n,m} e^{j2\pi k_\Delta n/N} e^{j\phi_m} \right) e^{j\frac{\pi}{N}(n-k)^2} \\ &= e^{j\phi_m} e^{-j\frac{\pi}{4}} \sum_{n=0}^{N-1} x_{n,m} e^{j\frac{\pi}{N}(n^2-2n(k-k_\Delta)+k^2)}. \end{aligned} \quad (6)$$

Knowing that

$$n^2 - 2nk + k^2 + 2nk_\Delta = [n - (k - k_\Delta)]^2 + 2kk_\Delta - k_\Delta^2, \quad (7)$$

it is possible to rewrite (6) as

$$\dot{Y}_{k,m} = e^{j\phi_m} e^{j\frac{\pi}{N}(2kk_\Delta - k_\Delta^2)} e^{-j\frac{\pi}{4}} \sum_{n=0}^{N-1} x_{n,m} e^{j\frac{\pi}{N}[n - (k - k_\Delta)]^2}. \quad (8)$$

Expressing $x_{n,m}$ as the IDFNT of $\dot{X}_{\kappa,m}$ in (8) and rearranging the resulting expression yields

$$\dot{Y}_{k,m} = \frac{e^{j\phi_m}}{N} \sum_{\kappa=0}^{N-1} \dot{X}_{\kappa,m} e^{j\frac{\pi}{N}(k^2 - \kappa^2)} \sum_{n=0}^{N-1} e^{j\frac{\pi}{N}n(-2k+2k_\Delta+2\kappa)}, \quad (9)$$

for $\kappa \in \{0, 1, \dots, N-1\}$. The rightmost sum in (9) is a finite geometric series, which, according to the result from the Appendix, can be evaluated to yield

$$\dot{Y}_{k,m} = \frac{e^{j\phi_m}}{N} \sum_{\kappa=0}^{N-1} \dot{X}_{\kappa,m} e^{j\frac{\pi}{N}(k^2 - \kappa^2)} \left(\frac{e^{j2\pi(k_\Delta - k + \kappa)} - 1}{e^{j\frac{2\pi}{N}(k_\Delta - k + \kappa)} - 1} \right). \quad (10)$$

Since $k \in \mathbb{N}$ and $\kappa \in \mathbb{N}$, it holds for the specific case where $k_\Delta \in \mathbb{Z}$, which is when the frequency shift f_Δ is an integer multiple of B/N , that

$$\left. \frac{e^{j2\pi(k_\Delta - k + \kappa)} - 1}{e^{j\frac{2\pi}{N}(k_\Delta - k + \kappa)} - 1} \right|_{k_\Delta \in \mathbb{Z}} = \delta[\langle \kappa - (k - k_\Delta) \rangle_N]. \quad (11)$$

The result from (11) finally allows rewriting (10) as

$$\dot{Y}_{k,m} = \frac{e^{j\phi_m}}{N} \sum_{\kappa=0}^{N-1} \dot{X}_{\kappa,m} e^{j\frac{\pi}{N}(k^2 - \kappa^2)} \delta[\langle \kappa - (k - k_\Delta) \rangle_N], \quad (12)$$

which after further manipulation becomes

$$\dot{Y}_{k,m} = e^{j\phi_m} \dot{X}_{\langle k - k_\Delta \rangle_N, m} e^{j\frac{\pi}{N}(2kk_\Delta - k_\Delta^2)}. \quad (13)$$

In summary, the results from (10) and (13) reveal that a frequency shift f_Δ during the propagation of the transmit OCDM signal through a channel results in a circular shift by $k_\Delta = f_\Delta/B$ samples and a multiplication by the complex exponential $e^{j\frac{\pi}{N}(2kk_\Delta - k_\Delta^2)}$ that rotates the phases of the elements within the columns of $\dot{\mathbf{Y}}$, which represent discrete-Fresnel domain receive OCDM symbols. Additionally, the introduced frequency shift rotates the phase of each m th OCDM symbol with respect to the previous one, which is expressed as the phase ϕ_m of the complex exponential $e^{j\phi_m}$ that multiplies all elements of the m th column of $\dot{\mathbf{Y}}$.

B. Effects of time shifts in the discrete-Fresnel domain

Let an OCDM signal be transmitted through a channel with a CIR represented in the discrete-time domain by \mathbf{h} . In the absence of frequency shifts, the columns of the discrete-time domain receive OCDM frame after CP removal \mathbf{y} are the result of the circular convolution between the columns of \mathbf{x} and \mathbf{h} . In other words, the element at the n th row and m th column of \mathbf{y} is expressed as $y_{n,m} = x_{n,m} \circledast h_n$, where \circledast is the circular convolution operator. Alternatively, one can write

$$y_{n,m} = \sum_{\nu=0}^{N-1} h_{\nu} x_{\langle n-\nu \rangle_N, m}, \quad (14)$$

for $\nu \in \{0, 1, \dots, N-1\}$.

By performing column-wise DFNTs on \mathbf{y} , the matrix representation $\dot{\mathbf{Y}}$ of the discrete-Fresnel domain frame is yielded. Its element at the k th row and m th column is expressed as

$$\dot{Y}_{k,m} = e^{-j\frac{\pi}{4}} \sum_{n=0}^{N-1} \left(\sum_{\nu=0}^{N-1} h_{\nu} x_{\langle n-\nu \rangle_N, m} \right) e^{j\frac{\pi}{8}(n-k)^2}. \quad (15)$$

Substituting $l = \langle n-\nu \rangle_N$ in (15) and rearranging the resulting expression yields (16). Based on the obtained results in Subsection II-A, more specifically in (10), (16) can be rewritten as in (17). Since $k \in \mathbb{N}$, $\kappa \in \mathbb{N}$, and $\nu \in \mathbb{N}$, the same principle from (11) can be applied to the rightmost term in (17), which then becomes (18). After further manipulation, (18) can be finally rewritten as

$$\dot{Y}_{k,m} = \sum_{\nu=0}^{N-1} h_{\nu} \dot{X}_{\langle k-\nu \rangle_N, m} \quad (19)$$

The relationship between $\dot{Y}_{k,m}$ and $\dot{X}_{k,m}$ as in (19) reveals that the same circular shifts and amplitude weightings suffered by the columns of \mathbf{x} are observed in the columns of both \mathbf{y} and its discrete-Fresnel domain representation $\dot{\mathbf{Y}}$. In other words, $y_{n,m} = x_{n,m} \circledast h_n$ results in $\dot{Y}_{k,m} = \dot{X}_{k,m} \circledast h_k$, which is also known as the convolution theorem of the DFNT [9], [16].

C. Joint effects of time and frequency shifts in the discrete-Fresnel domain

Should the propagation of the OCDM transmit signal through a channel results not only in time shifts represented by the CIR \mathbf{h} , but also in a normalized frequency shift k_{Δ} , the element at the n th row and m th column of the discrete-time domain receive frame \mathbf{y} obtained after CP removal at the receiver side can be expressed as

$$y_{n,m} = (x_{n,m} \circledast h_n) e^{j2\pi k_{\Delta} n/N} e^{j\phi_m}. \quad (20)$$

For the sake of simplicity, the auxiliary matrix $\mathbf{r} \in \mathbb{C}^{N \times M}$ is defined, being the element $r_{n,m} \in \mathbb{C}$ located at its n th row and m th column given by

$$r_{n,m} \triangleq x_{n,m} \circledast h_n. \quad (21)$$

Consequently, (20) can be alternatively expressed as

$$y_{n,m} = r_{n,m} e^{j2\pi k_{\Delta} n/N} e^{j\phi_m}. \quad (22)$$

Defining $\dot{\mathbf{R}} \in \mathbb{C}^{N \times M}$ as the output of column-wise DFNTs on \mathbf{r} , the relationship between the element $\dot{R}_{k,m} \in \mathbb{C}$ at the k th row and m th column of $\dot{\mathbf{R}}$ and the element $\dot{X}_{k,m}$ at the same position of $\dot{\mathbf{X}}$ can be defined based on the result from (18). Additionally, the element $\dot{Y}_{k,m}$ at the k th row and m th column of $\dot{\mathbf{Y}}$ can be derived from $\dot{R}_{k,m}$ based on the result from (10). Consequently, $\dot{Y}_{k,m}$ can be expressed as a function of $\dot{X}_{k,m}$ as in (23). In the specific case where $k_{\Delta} \in \mathbb{Z}$, the property used in (11) can be finally applied to (23), yielding

$$\dot{Y}_{k,m} = e^{j\phi_m} \left(\sum_{\nu=0}^{N-1} h_{\nu} \dot{X}_{\langle (k-k_{\Delta})-\nu \rangle_N, m} \right) e^{j\frac{\pi}{8}(2kk_{\Delta}-k_{\Delta}^2)}, \quad (24)$$

i.e., $\dot{Y}_{k,m} = e^{j\phi_m} (\dot{X}_{\langle k-k_{\Delta} \rangle_N, m} \circledast h_k) e^{j\frac{\pi}{8}(2kk_{\Delta}-k_{\Delta}^2)}$.

The results from (23) and (24) indicate that the convolution with the CIR followed by a frequency shift f_{Δ} during the propagation of the transmit OCDM signal through a channel results in a circular shift by $k_{\Delta} = f_{\Delta}/B$ samples on top of the circular shifts caused by the convolution with the

$$\dot{Y}_{k,m} = \sum_{\nu=0}^{N-1} h_{\nu} e^{j\frac{\pi}{8}(\nu^2-2\nu k)} e^{-j\frac{\pi}{4}} \sum_{l=0}^{N-1} \left(x_{l,m} e^{j2\pi\nu l/N} \right) e^{j\frac{\pi}{8}(l-k)^2}. \quad (16)$$

$$Y_{k,m} = \sum_{\nu=0}^{N-1} h_{\nu} e^{j\frac{\pi}{8}(\nu^2-2\nu k)} \left[\frac{1}{N} \sum_{\kappa=0}^{N-1} \dot{X}_{\kappa,m} e^{j\frac{\pi}{8}(k^2-\kappa^2)} \left(\frac{e^{j2\pi(\nu-k+\kappa)} - 1}{e^{j\frac{2\pi}{N}(\nu-k+\kappa)} - 1} \right) \right] \quad (17)$$

$$\dot{Y}_{k,m} = \sum_{\nu=0}^{N-1} h_{\nu} e^{j\frac{\pi}{8}(\nu^2-2\nu k)} \left(\frac{1}{N} \sum_{\kappa=0}^{N-1} \dot{X}_{\kappa,m} e^{j\frac{\pi}{8}(k^2-\kappa^2)} \delta(\langle \kappa - (k-\nu) \rangle_N) \right) \quad (18)$$

$$\dot{Y}_{k,m} = \frac{e^{j\phi_m}}{N} \sum_{\kappa=0}^{N-1} \left(\sum_{\nu=0}^{N-1} h_{\nu} \dot{X}_{\langle \kappa-\nu \rangle_N, m} \right) e^{j\frac{\pi}{8}(k^2-\kappa^2)} \left(\frac{e^{j2\pi(k_{\Delta}-k+\kappa)} - 1}{e^{j\frac{2\pi}{N}(k_{\Delta}-k+\kappa)} - 1} \right) \quad (23)$$

multiple taps of the discrete-time domain CIR representation \mathbf{h} . This effect is similar to known range- or delay-Doppler coupling in chirp-based radar systems [29]. Besides the aforementioned effect, a multiplication by the complex exponential $e^{j\frac{\pi}{N}(2kk_{\Delta}-k_{\Delta}^2)}$ of the shifted versions of $\dot{\mathbf{X}}$ takes place as observed in Subsection II-A, increasingly rotating the phases of the N elements of each column of $\dot{\mathbf{Y}}$. As in the case of Subsection II-A, every m th column of $\dot{\mathbf{Y}}$ is additionally multiplied by the complex exponential $e^{j\phi_m}$, which rotates the phase of all elements of the m th discrete-Fresnel domain OCDM symbol. The aforementioned effects ultimately distort the transmit subchirps and cause IChI in the discrete-Fresnel domain, which is somewhat similar to the ICI in the discrete-frequency domain in OFDM-based systems.

III. DISCRETE-FRESNEL DOMAIN CHANNEL ESTIMATION IN OCDM-BASED RADAR SYSTEMS

The discussion in Section II described the effects of time and frequency shifts on the originally transmitted discrete-Fresnel domain OCDM symbols represented by the columns of $\dot{\mathbf{X}}$, which becomes $\dot{\mathbf{Y}}$ after considering the effects of the propagation through a channel. Based on the achieved results, it is possible to predict the relationship between the channel estimates in OCDM-based systems and the actual channel CIR.

For this purpose, the discrete-Fresnel domain pilot design strategy introduced in [21] for coherent optical OFDM systems, which was also investigated for reflectometric sensing of power lines in baseband OCDM systems as reported in [24] and further improved in [22], is considered. The original pilot design from [21] performs unbiased channel estimation under the assumption that no frequency shifts take place. This is done by exploiting the convolution theorem of the DFnT [16] and having a Kronecker comb with $P \in \mathbb{N}_+$ active subchirps in the discrete-Fresnel domain at the transmitter side, and averaging the resulting P sections of length N/P in the discrete-Fresnel domain at the receiver side to estimate the CIR. Conversely, the improvement proposed in [22] achieves optimal CIR estimates in the minimum mean square error (MMSE) sense by activating only the first subchirp in the discrete-Fresnel domain at the transmitter side, and discarding noisy samples beyond the maximum expected CIR length N_{h} in the obtained discrete-Fresnel domain receive OCDM symbol to obtain a CIR estimate. Since dividing the transmission power among P active subchirps and averaging their corresponding CIR estimates yields the same SNR as in the case where the full transmission power is allocated to a single subchirp and only one CIR is obtained, the superiority of the improved pilot design approach is solely due to the noise-rejection windowing performed in the discrete-Fresnel domain at the receiver side.

Considering the two aforementioned characteristics of the pilot design strategies, namely the one from [21] and the one from [22], the latter one is adopted in this study. Consequently,

the element at the k th row and m th column of the matrix $\dot{\mathbf{X}}$ that represents a frame containing M discrete-Fresnel domain pilot OCDM symbols in its columns is given by

$$\dot{X}_{k,m} = \delta[k]. \quad (25)$$

As all M OCDM symbols within the frame are equal, no CP is required. The implications of the pilot OCDM symbol design on the performance of radar channel estimation is analyzed in Subsection III-A. Furthermore, extensions of the discussed concept to MU or MIMO scenarios as well as to RadCom applications are discussed in Subsections III-B and III-C, respectively.

A. Radar Channel Estimation

For the sake of simplicity, it is assumed in this subsection that the OCDM-based system acts as a monostatic radar, in which transmit and receive antennas are virtually collocated. In practice, however, only a quasi-monostatic radar is possible, in which the distance between transmit and receive antennas is negligible in comparison to the range of expected target distances w.r.t. the radar. To estimate the range and relative radial velocity of multiple point targets w.r.t. the radar, consecutive radar CIRs are estimated. Each CIR is composed of multiple taps at delays corresponding to the time of flight (ToF) taken by the OCDM signal to be sent out by the transmit antenna, reflected off targets, and captured by the receive antenna. If no effects such as range migration occur within the measurement time, all of the estimated radar CIRs allow estimating the range of resolved point targets present in the monitored scenario. The observed difference among consecutive CIRs, which is the phase progression of its taps, ultimately allows obtaining a radar image that has not only range information, but also estimates of the experienced Doppler shifts related to the relative radial velocities of the point targets. To enable the aforementioned estimation of range and Doppler shifts of $H \in \mathbb{N}$ point targets, the matrix $\tilde{\mathbf{y}}^{\text{rad}} \in \mathbb{C}^{N \times M}$ that would ideally represent the discrete-time domain receive OCDM frame has elements at its n th row and m th column expressed as in (26). In this equation, $n_{\Delta,\eta} \in \mathbb{R} | n_{\Delta,\eta} = 2R_{\eta}B/c_0$ is a normalized range term, being $R_{\eta} \in \mathbb{R}_+$ the range in meters of the η th target and c_0 the speed of light in vacuum in meters per second. Additionally, $k_{\Delta,\eta} \in \mathbb{R}$ and $\phi_{m,\eta} \in \mathbb{R}$ are the normalized Doppler shift and the Doppler phase associated to the η th point target. In the specific case where $n_{\Delta,\eta} \in \mathbb{Z}$, (26) can be rewritten as

$$\tilde{y}_{n,m}^{\text{rad}} = \sum_{\eta=0}^{H-1} x_{n,m} \delta[n - n_{\Delta,\eta}] e^{j2\pi k_{\Delta,\eta} n/N} e^{j\phi_{m,\eta}}. \quad (27)$$

With the OCDM pilot symbols contained in the columns of $\dot{\mathbf{X}}$ having their k th elements defined as in (25), the resulting ideal discrete-Fresnel domain receive OCDM frame

$$\tilde{\mathbf{y}}_{n,m}^{\text{rad}} = \sum_{\eta=0}^{H-1} \left[\sum_{\nu=0}^{N-1} x_{\nu,m} \left(\frac{e^{j2\pi(n_{\Delta,\eta}-n+\nu)} - 1}{e^{j\frac{2\pi}{N}(n_{\Delta,\eta}-n+\nu)} - 1} \right) \right] e^{j2\pi k_{\Delta,\eta} n/N} e^{j\phi_{m,\eta}} \quad (26)$$

matrix representation $\tilde{\mathbf{Y}}^{\text{rad}}$ can be alternatively defined as the matrix $\tilde{\mathbf{h}}^{\text{rad}} \in \mathbb{C}^{N \times M}$ that contains M consecutive radar CIR estimates of length N , which can be expressed as

$$\tilde{h}_{n,m}^{\text{rad}} = \sum_{\eta=0}^{H-1} \left(\frac{e^{j2\pi(n_{\Delta,\eta}-n)} - 1}{e^{j\frac{2\pi}{N}(n_{\Delta,\eta}-n)} - 1} \right) e^{j2\pi k_{\Delta,\eta} n/N} e^{j\phi_{m,\eta}} \quad (28)$$

or simply

$$\tilde{h}_{n,m}^{\text{rad}} = \sum_{\eta=0}^{H-1} \delta[n - n_{\Delta,\eta}] e^{j2\pi k_{\Delta,\eta} n/N} e^{j\phi_{m,\eta}} \quad (29)$$

for $n_{\Delta,\eta} \in \mathbb{Z}$.

In reality, however, a matrix $\mathbf{Y}^{\text{rad}} \in \mathbb{C}^{N \times M} | \mathbf{Y}^{\text{rad}} \neq \tilde{\mathbf{Y}}^{\text{rad}}$ is obtained at the receiver side of the OCDM-based system. Since pilot OCDM symbols are transmitted, \mathbf{Y}^{rad} can be alternatively defined as the matrix $\hat{\mathbf{h}}^{\text{rad}} \in \mathbb{C}^{N \times M} | \hat{\mathbf{h}}^{\text{rad}} \neq \tilde{\mathbf{h}}^{\text{rad}}$ that contains the actual consecutive radar CIR estimates in its columns. Assuming a single target scenario and considering only the m th of the M radar channel estimates, a corresponding continuous-frequency domain channel frequency response (CFR) $\hat{H}_m^{\text{rad}}(f) \in \mathbb{C}$ of the aforementioned channel presents linear phase progression along with the frequency in the RF band $f \in [f_c - B/2, f_c + B/2]$ as represented at the top of Fig. 1. In the discrete-frequency domain, the CIR contained in the m th column of $\hat{\mathbf{h}}^{\text{rad}}$ is represented by the vector $\hat{\mathbf{H}}_m^{\text{rad}} \in \mathbb{C}^{N \times 1}$. Since the samples $k = 0$ to $k = N/2 - 1$ of $\hat{\mathbf{H}}_m^{\text{rad}}$ can be used to reconstruct spectral information on the RF frequencies f_c to $f_c + (N/2 - 1)B/N = f_c + B/2 - B/N$, while the samples $k = N/2 + 1$ to $k = N$ allow reconstructing spectral information on the frequencies $f_c + (-N/2)B/N = f_c - B/2$ to $f_c - B/N$, the phase of $\hat{\mathbf{H}}_m^{\text{rad}}$ is circularly shifted by $N/2$ samples w.r.t. an ideally linearly increasing phase [30]. Considering a single-target scenario, an exemplary phase progression in the baseband (BB) of $\hat{\mathbf{H}}_m^{\text{rad}}$ can be seen in Fig. 1.

In order for the ToFs, and consequently target ranges, to be appropriately estimated, the effectively obtained matrix $\mathbf{y}^{\text{rad}} \in \mathbb{C}^{N \times M} | \mathbf{y}^{\text{rad}} \neq \tilde{\mathbf{y}}^{\text{rad}}$ that represents the discrete-time domain receive OCDM frame must consist of circularly-shifted versions of \mathbf{x} . If the experienced phase folding is not compensated, the columns of the estimated radar CIR matrix $\hat{\mathbf{h}}^{\text{rad}}$ are equal to the corresponding columns of the ideally obtained matrix $\tilde{\mathbf{h}}^{\text{rad}}$ with the addition of discrete-frequency domain shift by $N/2$ samples. In other words

$$\hat{h}_{n,m}^{\text{rad}} = \tilde{h}_{n,m}^{\text{rad}} e^{-j2\pi(N/2)n/N} = \tilde{h}_{n,m}^{\text{rad}} e^{-j\pi n}, \quad (30)$$

where $\hat{h}_{n,m}^{\text{rad}}$ denotes the element of $\hat{\mathbf{h}}^{\text{rad}}$ at its n th row and m th column. Although the amplitudes of the elements of $\hat{\mathbf{h}}^{\text{rad}}$ are the same as the corresponding ones of $\tilde{\mathbf{h}}^{\text{rad}}$, the introduced phase rotations would ultimately prevent correctly estimating the ranges of targets when reconstructing the analog equivalent of $\hat{\mathbf{h}}^{\text{rad}}$, e.g., via zero padding (ZP). Consequently, the experienced phase folding must be corrected by performing a circular shift in the discrete-frequency domain by $N/2$ on \mathbf{Y}^{rad} to produce $\mathbf{Y}^{\text{rad,corr}} \in \mathbb{C}^{N \times M}$, which can be alternatively defined as the matrix $\hat{\mathbf{h}}^{\text{rad,corr}} \in \mathbb{C}^{N \times M}$ that contains an estimate of the desired radar CIR matrix $\tilde{\mathbf{h}}^{\text{rad}}$. The

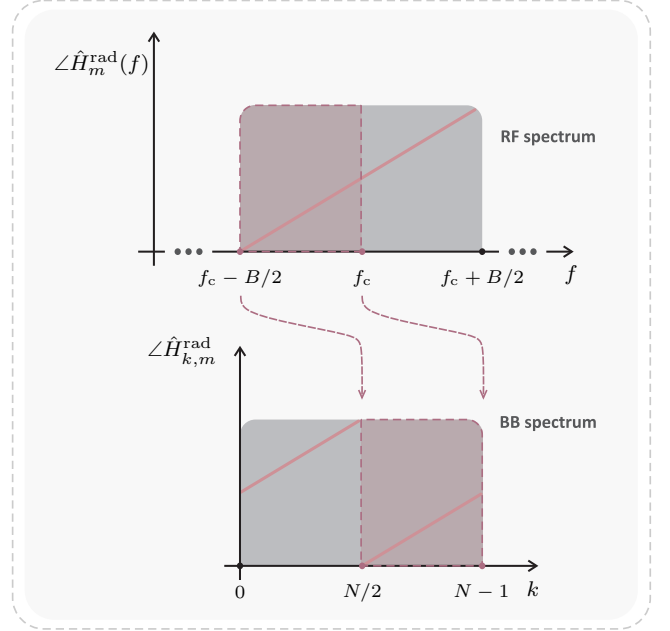


Fig. 1: Channel frequency response phase progression due to experienced propagation time delay in RF and BB spectra [30].

aforementioned phase folding compensation can be achieved in two manners. The first one is by multiplying every k th element of \mathbf{Y}^{rad} by $e^{j\pi k}$. A second solution is based on the OCDM receiver #2 structure from [9], where the DFNT is calculated by means of a discrete Fourier transform (DFT), followed by an element-wise multiplication by the vector $\mathbf{\Gamma} \in \mathbb{C}^{N \times 1} | \mathbf{\Gamma} = [\Gamma_0, \Gamma_1, \dots, \Gamma_{N-1}]^T$, whose k th element is expressed for even N as

$$\Gamma_k = e^{-j\pi k^2/N}, \quad (31)$$

and an inverse discrete Fourier transform (IDFT). In this approach, a circular shift in the discrete-frequency domain by $N/2$ samples is performed between the element-wise multiplication by $\mathbf{\Gamma}$ and the IDFT.

Assuming that no Doppler shifts take place, i.e., $k_{\Delta,\eta} = 0$ and $\phi_{m,\eta} = 0 \forall m, \eta$, both described phase folding correction approaches yield the CIR matrix estimate $\hat{\mathbf{h}}^{\text{rad,corr}}$, whose element at its n th row and m th column is given by

$$\hat{h}_{n,m}^{\text{rad,corr}} = e^{j\pi n} \hat{h}_{n,m}^{\text{rad}} = \tilde{h}_{n,m}^{\text{rad}}. \quad (32)$$

If, however, a frequency shift also takes place, the discrete-time domain CIR matrix representation without phase folding correction $\hat{\mathbf{h}}^{\text{rad}}$ has the element at its n th row and m th column expressed as in (33) or, for the specific case where $n_{\Delta,\eta} \in \mathbb{Z}$ and $k_{\Delta,\eta} \in \mathbb{Z} \forall \eta$, as in (34). After performing phase folding correction, $\hat{\mathbf{h}}^{\text{rad,corr}}$ is obtained such that the element in its n th row and m th column is expressed as in (35) or, for $n_{\Delta,\eta} \in \mathbb{Z}$ and $k_{\Delta,\eta} \in \mathbb{Z} \forall \eta$, as in (36).

The obtained expressions in (35) and (36) reveal that the delay-Doppler coupling mentioned in Subsection II-C still takes place after phase folding correction. Additionally, it is observed for the η th target contribution to the aforementioned equations that the columns of $\hat{\mathbf{h}}^{\text{rad,corr}}$ are circularly-shifted versions of the columns of $\tilde{\mathbf{h}}^{\text{rad}}$ by $k_{\Delta,\eta}$ samples. Compared to

$$\begin{aligned}\hat{h}_{n,m}^{\text{rad}} &= \sum_{\eta=0}^{H-1} \frac{e^{j\phi_{m,\eta}}}{N} \sum_{\kappa=0}^{N-1} \left[\sum_{\nu=0}^{N-1} \left(\frac{e^{j2\pi(n_{\Delta,\eta}-\nu)} - 1}{e^{j\frac{2\pi}{N}(n_{\Delta,\eta}-\nu)} - 1} \right) e^{-j\pi\nu} \delta[\langle \kappa - \nu \rangle_N] \right] e^{j\frac{\pi}{N}(n^2-\kappa^2)} \left(\frac{e^{j2\pi(k_{\Delta,\eta}-n+\kappa)} - 1}{e^{j\frac{2\pi}{N}(k_{\Delta,\eta}-n+\kappa)} - 1} \right) \\ &= \sum_{\eta=0}^{H-1} \frac{e^{j\phi_{m,\eta}}}{N} \sum_{\kappa=0}^{N-1} \left[\left(\frac{e^{j2\pi(n_{\Delta,\eta}-\kappa)} - 1}{e^{j\frac{2\pi}{N}(n_{\Delta,\eta}-\kappa)} - 1} \right) e^{-j\pi\kappa} \right] e^{j\frac{\pi}{N}(n^2-\kappa^2)} \left(\frac{e^{j2\pi(k_{\Delta,\eta}-n+\kappa)} - 1}{e^{j\frac{2\pi}{N}(k_{\Delta,\eta}-n+\kappa)} - 1} \right)\end{aligned}\quad (33)$$

$$\begin{aligned}\hat{h}_{n,m}^{\text{rad}} &= \sum_{\eta=0}^{H-1} e^{j\phi_{m,\eta}} \delta[\langle n - (n_{\Delta,\eta} + k_{\Delta,\eta}) \rangle_N] e^{-j\pi[n - (n_{\Delta,\eta} + k_{\Delta,\eta})]} e^{j\frac{\pi}{N}(n^2 - (n - k_{\Delta,\eta})^2)} \\ &= \sum_{\eta=0}^{H-1} e^{j\phi_{m,\eta}} \delta[\langle n - (n_{\Delta,\eta} + k_{\Delta,\eta}) \rangle_N] e^{-j\pi[n - (n_{\Delta,\eta} + k_{\Delta,\eta})]} e^{j\frac{\pi}{N}(2nk_{\Delta,\eta} - k_{\Delta,\eta}^2)}\end{aligned}\quad (34)$$

$$\hat{h}_{n,m}^{\text{rad,corr}} = e^{j\pi n} \hat{h}_{n,m}^{\text{rad}} = e^{j\pi n} \left\{ \sum_{\eta=0}^{H-1} \frac{e^{j\phi_{m,\eta}}}{N} \sum_{\kappa=0}^{N-1} \left[\left(\frac{e^{j2\pi(n_{\Delta,\eta}-\kappa)} - 1}{e^{j\frac{2\pi}{N}(n_{\Delta,\eta}-\kappa)} - 1} \right) e^{-j\pi\kappa} \right] e^{j\frac{\pi}{N}(n^2-\kappa^2)} \left(\frac{e^{j2\pi(k_{\Delta,\eta}-n+\kappa)} - 1}{e^{j\frac{2\pi}{N}(k_{\Delta,\eta}-n+\kappa)} - 1} \right) \right\} \quad (35)$$

$$\hat{h}_{n,m}^{\text{rad,corr}} = e^{j\pi n} \hat{h}_{n,m}^{\text{rad}} = \sum_{\eta=0}^{H-1} e^{j\phi_{m,\eta}} \delta[\langle n - (n_{\Delta,\eta} + k_{\Delta,\eta}) \rangle_N] e^{j\frac{\pi}{N}[2nk_{\Delta,\eta} - k_{\Delta,\eta}^2 + N(n_{\Delta,\eta} + k_{\Delta,\eta})]} \quad (36)$$

their counterparts in $\tilde{\mathbf{h}}^{\text{rad}}$, the n th elements of the aforementioned columns are also multiplied by complex exponentials with linearly increasing phase along with the index n .

Since each of the M columns of $\hat{\mathbf{h}}^{\text{rad,corr}}$ contains information on the range of the H targets, performing row-wise DFTs on $\hat{\mathbf{h}}^{\text{rad,corr}}$ converts the phases $\phi_{m,\eta}$ into Doppler shift information. The aforementioned processing produces the matrix $\mathbf{I}^{\text{rad}} \in \mathbb{C}^{N \times M}$, which allows to clearly extract information on the range and relative radial velocity of all H targets if they are resolved in at least one of the radar image dimensions. Based on the analyses in [3], [12], [13], [31], the aforementioned radar image experiences a processing gain G_p and is associated with range resolution ΔR and maximum unambiguous range $R_{\text{max,ua}}$, as well as relative radial velocity resolution Δv and maximum unambiguous relative radial velocity $v_{\text{max,ua}}$ values as shown in Table I. Since all transmit OCDM symbols within the frame are equal and therefore no CP is required, no further restriction on the maximum range value such as in [3], [12], and [13] is considered. Furthermore, since a restriction on the maximum tolerable relative radial velocity for the considered OCDM-based system will be accurately investigated in Section IV, it is not listed in Table I.

B. Extension to MU or MIMO Radar Operation

If $P \in \mathbb{N}_+$ synchronized OCDM radar transmitters labeled as $p \in \{0, 1, \dots, P-1\}$ are to operate simultaneously in a MU or MIMO scenario, then the elements of the matrix $\hat{\mathbf{X}}^P \in \mathbb{C}^{N \times M}$ that represents the discrete-Fresnel domain transmit frame of the p th transmitter are given by

$$\hat{X}_{k,m}^P = \delta[\langle k - pN/P \rangle_N]. \quad (37)$$

TABLE I: Performance parameters in an OCDM-based radar system with discrete-Fresnel domain channel estimation. If all OCDM symbols within the frame are equal, no CP is needed and therefore N_{CP} can be set to zero.

Radar performance parameters	
Processing gain	$G_p = NM$
Range resolution	$\Delta R = c_0/(2B)$
Max. unamb. range	$R_{\text{max,ua}} = N c_0/(2B)$
Velocity resolution	$\Delta v = B c_0/[2f_c(N + N_{\text{CP}})M]$
Max. unamb. velocity	$v_{\text{max,ua}} = B c_0/[4f_c(N + N_{\text{CP}})]$

This equation indicates that the FrDM scheme [12], which was originally proposed in [24] for distributed reflectometric sensing of power lines, is adopted to enable orthogonal transmission of signals associated with each of the P transmitters as depicted in Fig. 2.

Assuming that there are $Q \in \mathbb{N}_+$ synchronized OCDM radar receivers labeled as $q \in \{0, 1, \dots, Q-1\}$ and following the formulation in Section III-A, the elements of the matrix $\hat{\mathbf{Y}}^q \in \mathbb{C}^{N \times M}$ representing the receive frame of the q th receiver are given by

$$\hat{Y}_{k,m}^q = \sum_{p=0}^{P-1} \hat{h}_{\langle k-pN/P \rangle_N, m}^{\text{rad,corr,p,q}}, \quad (38)$$

where $\hat{h}_{k,m}^{\text{rad,corr,p,q}} \in \mathbb{C}$ is the element at the k th row and m th column of the matrix $\hat{\mathbf{h}}^{\text{rad,corr,p,q}} \in \mathbb{C}^{N \times M}$ that represents consecutive CIR estimates associated with the p th transmitter and q th receiver. If the CIRs in $\hat{\mathbf{h}}^{\text{rad,corr,p,q}}$ are assumed to have length equal to or smaller than N/P , i.e., $\hat{\mathbf{h}}^{\text{rad,corr,p,q}}$ can be redefined as $\hat{\mathbf{h}}^{\text{rad,corr,p,q}} \in \mathbb{C}^{N/P \times 1}$, than its elements

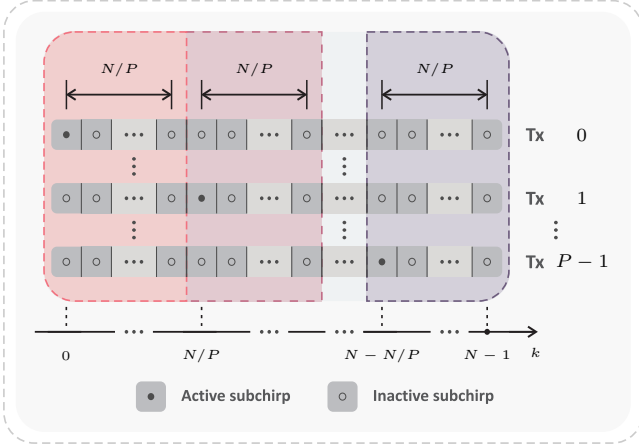


Fig. 2: Subchirp allocation in the discrete-Fresnel domain among distinct transmit channels for MU or MIMO operation based on FrDM.

$\hat{h}_{k',m}^{\text{rad,corr,p,q}} \in \mathbb{C}$, $k' \in \{0, 1, \dots, N/P - 1\}$, can be extracted from $\hat{\mathbf{Y}}^q$ as

$$\hat{h}_{k',m}^{\text{rad,corr,p,q}} = \hat{\mathbf{Y}}_{k'+pN/P,m}^q. \quad (39)$$

With the described FrDM approach for enabling MU or MIMO radar operation, most performance parameters from Table I are kept as all OCDM symbols in the transmit frame are equal and CPs are not needed. The only exception is the maximum unambiguous range, which becomes $R_{\text{max,ua}}^{\text{MU/MIMO,P}} = (N/P) c_0/(2B)$. It is worth highlighting that, although the ultimately obtained CIR estimates have the reduced length of N/P , the processing gain remains proportional to N since it is already experienced after the DFNT at the receiver, which performs a pulse-compression like operation on the N discrete-time domain samples and takes place before the N/P samples associated with each transmitter are selected at each receiver.

C. Extension to RadCom Operation

To enable joint RadCom operation of an OCDM-based radar system with discrete-Fresnel domain estimation, the FrDM principle explained in Section III-B is applied. In this context, a sector-modulated OCDM symbol structure in the discrete-Fresnel domain based on the autocorrelation pattern of zero correlation zone (ZCZ) sequences used in PMCW radars is adopted. Unlike in the radar-only case from Section III-A, each of the M OCDM symbols in the transmit frame will be unique as they carry different modulated data. Consequently, a CP of length $N_{\text{CP}} \in \mathbb{N}_+ \setminus \{2N_{\text{CP}} - 1 < N\}$ must be appended to each OCDM symbol in the discrete-time domain to avoid ISI. The resulting maximum tolerable range in the considered OCDM-based RadCom system is $R_{\text{max,CP}} = N_{\text{CP}} c_0/(2B)$, which is assumed to be lower than the maximum unambiguous range $R_{\text{max,ua}}$ listed in Table I.

For a given N_{CP} , the FrDM-based design of the OCDM symbol depicted in Fig. 3 is adopted and described as follows. First, the active, unmodulated subchirp of index $k = 0$ from (25) is kept and allocated and energy $\mathcal{E}^{\text{Rad}} \in \mathbb{R}_+$, being followed by $N_{\text{CP}} - 1$ inactive subchirps. At the receiver side, these first N_{CP} elements of the discrete-Fresnel domain OCDM symbol will ultimately contain the radar CIR estimate. Next, subchirps $k = N_{\text{CP}}$ to $k = N - N_{\text{CP}} + 1$, which comprise a total of $N - 2N_{\text{CP}} + 1$ subchirps, are modulated with symbols belonging to a digital modulation constellation that are contained in the matrix $\mathbf{C} \in \mathbb{C}^{(N-2N_{\text{CP}}+1) \times M}$. Finally, the last $N_{\text{CP}} - 1$ are kept inactive, which, taking into account energy factors unlike in the previous sections, yields a discrete-Fresnel domain transmit frame whose elements are given by

$$\begin{aligned} \dot{X}_{k,m} &= \sqrt{\mathcal{E}^{\text{Rad}}} \delta[k] \\ &+ \sum_{k''=0}^{(N-2N_{\text{CP}}+1)-1} C_{k'',m} \delta[\langle k - (N_{\text{CP}} + k'') \rangle_N]. \end{aligned} \quad (40)$$

In this equation, $k'' \in \{0, 1, \dots, (N - 2N_{\text{CP}} + 1) - 1\}$ and $C_{k'',m}$ denotes an element of $\mathbf{C} \in \mathbb{C}^{(N-2N_{\text{CP}}+1) \times M}$, which belongs to a digital modulation constellation with mean constellation energy that can be expressed as $\mathcal{E}^{\text{Com}} = \mathbb{E}\{|C_{k'',m}|^2\}$ if $C_{k'',m}$ is regarded as a random variable. The total energy allocated to the transmit OCDM symbol for joint RadCom operation is consequently $\mathcal{E}^{\text{RadCom}} = \mathcal{E}^{\text{Rad}} + (N - 2N_{\text{CP}} + 1)\mathcal{E}^{\text{Com}}$. The last $N_{\text{CP}} - 1$ inactive subchirps of each OCDM symbol are used as a guard interval to avoid interference of the $N - 2N_{\text{CP}} + 1$ communication subchirps onto the N_{CP} radar subchirps, as the OCDM symbols experience a circular convolution with the radar CIRs. Due to the OCDM symbol structure from (40), the proposed OCDM-based RadCom system is named sector-modulated OCDM-based RadCom system.

After transmitted, the OCDM RadCom signal will not only reflect off radar targets and be received by the same OCDM RadCom system that originally transmitted it, but also propagate towards another OCDM communication or RadCom device. The radar case is first explained as follows. Assuming $n_{\Delta,\eta} \in \mathbb{Z}$ and $k_{\Delta,\eta} \in \mathbb{Z}$ for the sake of conciseness and using the result from (35), the elements of the matrix $\hat{\mathbf{Y}}^{\text{rad}} \in \mathbb{C}^{N \times M}$ representing the radar receive frame after CP removal and transformation into the discrete-Fresnel domain are expressed as in (41). Similarly, the result for $n_{\Delta,\eta} \in \mathbb{R}$ and $k_{\Delta,\eta} \in \mathbb{R}$ can be achieved based on the result from (36). Since the length of the CIRs in $\hat{\mathbf{Y}}^{\text{rad}}$ is equal to or smaller than N_{CP} , the aforementioned CIR matrix can be redefined as $\hat{\mathbf{Y}}^{\text{rad}} \in \mathbb{C}^{N_{\text{CP}} \times M}$. Based on both (41) and the sufficient guard interval composed by null subchirps at the end of the discrete-Fresnel domain OCDM symbols in (40), the elements

$$\hat{\mathbf{Y}}_{k,m}^{\text{rad,q}} = \hat{h}_{k,m}^{\text{rad,corr}} + \sum_{k''=0}^{(N-2N_{\text{CP}}+1)-1} C_{k'',m} \sum_{\eta=0}^{H-1} e^{j\phi_{m,\eta}} \delta[\langle k - (n_{\Delta,\eta} + N_{\text{CP}} + k_{\Delta,\eta}) \rangle_N] e^{j\frac{\pi}{N}[2nk_{\Delta,\eta} - k_{\Delta,\eta}^2 + N(n_{\Delta,\eta}k_{\Delta,\eta})]} \quad (41)$$

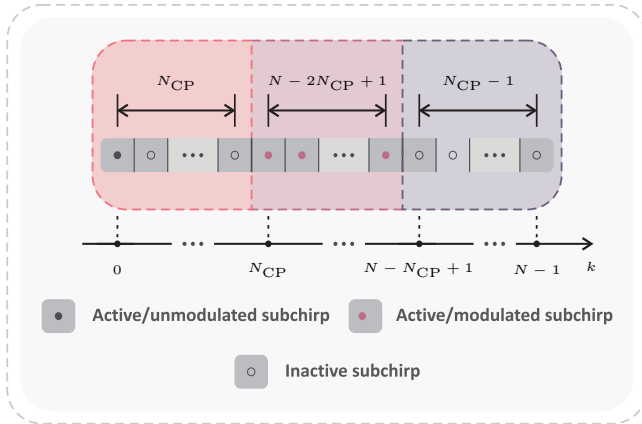


Fig. 3: Subchirp allocation in the discrete-Fresnel domain for enabling joint RadCom operation. The first active, unmodulated subchirp and the next $N_{CP} - 1$ inactive subchirps are used for radar sensing, while the $N - 2N_{CP} + 1$ active, modulated subchirps are used for communication. The last $N_{CP} - 1$ inactive subchirps are used as a guard interval.

$\hat{h}_{k''',m}^{\text{rad,corr}} \in \mathbb{C}$, $k''' \in \{0, 1, \dots, N_{CP} - 1\}$, of the aforementioned CIR matrix can be extracted from $\dot{\mathbf{Y}}^{\text{rad}} \in \mathbb{C}^{N \times M}$ as

$$\hat{h}_{k''',m}^{\text{rad,corr}} \approx \dot{Y}_{k''',m}^{\text{rad}}. \quad (42)$$

Apart from the aforementioned maximum range, all other radar performance parameters from Table I also hold for the considered sector-modulated OCDM-based RadCom system with discrete-Fresnel domain channel estimation.

As for the captured signal by the receiver of another OCDM communication or RadCom device, it is henceforth assumed that both timing and frequency synchronizations are ensured via techniques such as Schmidl & Cox's algorithm [26], [27]. After CP removal and transformation into the discrete-Fresnel domain, CIR estimates can be obtained from the same unmodulated pilot subchirps that used for radar sensing as previously mentioned. After channel equalization, the modulation symbols contained in subchirps $k = N_{CP}$ to $k = N - N_{CP} + 1$ can finally be extracted and demodulated following a typical OCDM processing chain.

IV. NUMERICAL AND MEASUREMENT RESULTS

In this section, a performance analysis of discrete-Fresnel domain channel estimation for OCDM-based radar systems is performed. Aiming at mid-range highly automated driving (HAD) applications [3], a carrier frequency $f_c = 79$ GHz and a frequency bandwidth $B = 1$ GHz are adopted. Additionally, $N = 2048$ subchirps, no CP, i.e., $N_{CP} = 0$, and $M = 5120$ OCDM symbols are considered unless explicitly stated otherwise, which results in an OCDM symbol time duration of $2.05 \mu\text{s}$, an OCDM frame time duration of 10.49 ms, and in the radar performance parameters listed in Table II.

Based on the aforementioned parameters, simulated peak power loss ratio (PPLR), peak sidelobe level ratio (PSLR), and integrated-sidelobe level ratio (ISLR) [3], [32] results are shown in Fig. 4 to assess the distortion of the range mainlobe and sidelobes induced by Doppler shifts. Since those calculations assume a single point target, the subindex η is henceforth

TABLE II: Resulting radar performance parameters in the considered OCDM-based radar system.

Radar performance parameters	
Processing gain	$G_p = 70.21$ dB
Range resolution	$\Delta R = 0.15$ m
Max. unamb. range	$R_{\text{max,ua}} = 307.20$ m
Velocity resolution	$\Delta v = 0.18$ m/s
Max. unamb. velocity	$v_{\text{max,ua}} = 463.56$ m/s

omitted for $n_{\Delta,\eta}$ and $k_{\Delta,\eta}$ for the sake of simplicity. In this figure, the whole unambiguous interval for range and relative radial velocity were considered, which results in $n_{\Delta} \in [0, 2048]$ and $k_{\Delta} \in [-0.5, 0.5]$. The values for k_{Δ} were defined based on the maximum unambiguous velocity expression from Table I, the relationship $f_D = 2v/\lambda = 2vf_c/c_0$ between Doppler shifts and relative radial velocities, and the frequency resolution $\Delta f = B/N$ of the OCDM-based radar system. Consequently, k_{Δ} can be interpreted as a normalized Doppler shift expressed as $k_{\Delta} = f_D/\Delta f$. Similarly, n_{Δ} can be interpreted as a normalized range by the range resolution and expressed as $n_{\Delta} = R/\Delta R$. Overall, degradations of PPLR, PSLR, and ISLR are mostly only observed for $|k_{\Delta}| > 0.1$, which is also expected, e.g., in OFDM-based radar and RadCom systems where the maximum tolerable velocity is associated with this k_{Δ} upper bound [3], [31]. The PPLR results in Fig. 4(a) show a highest degradation of the processing gain G_p of up to about 4 dB, e.g., for the approximate region covered by $n_{\Delta} \in [0, 767] \cup [1279, 2048]$ and $k_{\Delta} = -0.5$. Next, Fig. 4(b) shows the PSLR results, which indicate the ratio between the highest sidelobe and the mainlobe, while the ISLR results, which indicate the ratio between the integrated sidelobe level and the integrated mainlobe level, are presented in Fig. 4(c). Near the aforementioned region in the PPLR case, both PSLR and ISLR experience significant degradation, which can be explained by the results from (35) and (36). Besides the range-Doppler coupling in these equations, the range and Doppler dependent phase terms, which are $e^{j\frac{\pi}{N}(2nk_{\Delta,\eta} - k_{\Delta,\eta}^2 + Nk_{\Delta,\eta})}$ in (36), introduce changes in the shape of the estimated CIRs w.r.t. the ideally expected ones and is illustrated in more detail as follows.

Fig. 5 shows range-velocity radar images obtained from measurements with a Zynq UltraScale+ RFSoc ZCU111 from Xilinx, Inc. The aforementioned system-on-a-chip (SoC) platform was used to emulate both the OCDM-based radar system with the adopted parameters in this section and transmit power $P_{\text{Tx}} = 0$ dBm, as well as the radar target simulator (RTS) described in [33] for a single radar target with radar cross section (RCS) $\sigma_{\text{RCS}} = 30$ dBsm at 30 m ($n_{\Delta} = 200$) and velocities ranging from 0 m/s ($k_{\Delta} = 0$) to 463.56 m/s ($k_{\Delta} = -0.5$). In these images, it is possible to see that, for increasing radial relative velocities and consequently Doppler shifts, the aforementioned range-Doppler coupling and the range and Doppler dependent phase terms may bias the target reflection from its actual range and duplicate the target's reflection in the range direction if $k_{\Delta} = 0$, which explains

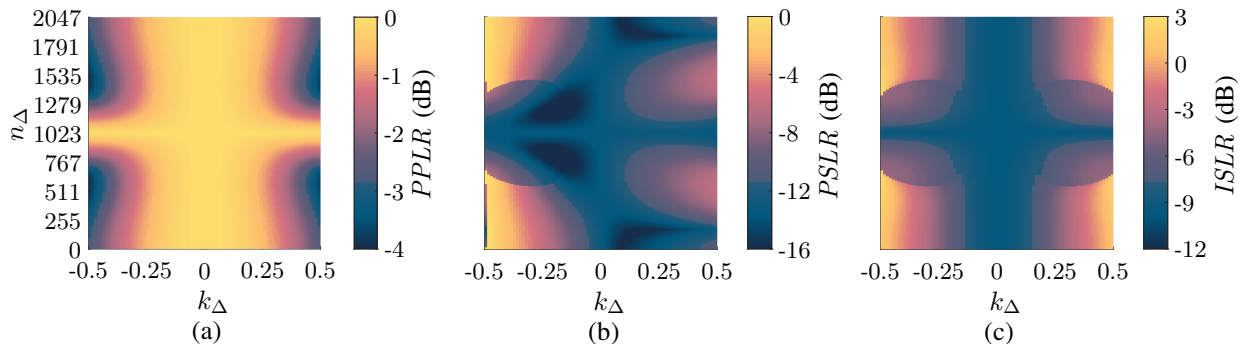


Fig. 4: Simulated Doppler-shift tolerance: (a) PPLR, (b) PSLR, and (c) ISLR of a single target reflection with different $n_{\Delta} = 2RB/c_0$ and $k_{\Delta} = f_D/\Delta f$ pairs obtained in an OCDM-based system with discrete-Fresnel domain radar processing.

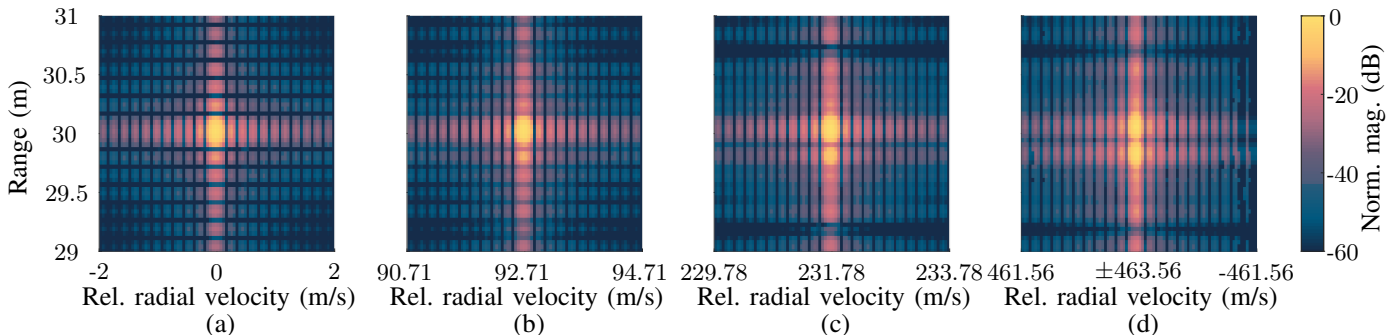


Fig. 5: Obtained range-velocity radar images from measurements with OCDM-based radar systems with discrete-Fresnel domain channel estimation for a single target with relative radial velocities of (a) 0 m/s ($k_{\Delta} = 0$), (b) 92.71 m/s ($k_{\Delta} = -0.1$), (c) 231.78 m/s ($k_{\Delta} = -0.25$), and (d) 463.56 m/s ($k_{\Delta} = -0.5$). In all radar images the actual target range is 30 m ($n_{\Delta} = 200$).

the PPLR, PSLR, and ISLR results from Fig. 4. Conversely, the Doppler shift or relative radial velocity estimation is not affected by the aforementioned effects and only depends on the Doppler-induced phases $e^{j\phi_{m,n}}$ in (35) and (36). As a consequence, similar performance for the velocity processing, e.g., to OFDM or PMCW radars is achieved.

For a more detailed visualization, Fig. 6 shows range cuts at the estimated target velocities of the measured radar images from Fig. 5 with a focus on the target’s range. Results for three additional systems parameterized to yield the same frame duration are shown for each considered velocity in Fig. 6 for the sake of comparison. The first are for the proposed sector-modulated OCDM-based RadCom system in Section III-C with $N = 2048$ subchirps, CP length of $N_{CP} = 512$, and $M = 4096$ OCDM symbols. The second set of results is for the conventional OCDM-based radar system from [13] with $N = 2048$ subchirps, $N_{CP} = 512$ CP length, and $M = 4096$ OCDM symbols. Finally, the third set of results is for an OFDM-based RadCom system with $N = 2048$ subcarriers, CP length of $N_{CP} = 512$, and $M = 4096$ OFDM symbols. For all three aforementioned modulation schemes, the resulting maximum tolerable range defined by the CP length is $R_{max,CP} = 76.8$ m, the achieved processing gain is $G_p = 69.24$ dB, and quadrature phase-shift keying (QPSK) modulation with uniform power allocation is adopted for the modulated subchirps or subcarriers. As shown in Fig. 6, the proposed OCDM-based radar system and its sector-modulated OCDM-based RadCom yield virtually equal radar range profiles. At zero Doppler shift, i.e., $k_{\Delta} = 0$, they yield

the same range profile result as their OFDM counterpart and a more regular sidelobe trend than the conventional OCDM-based RadCom system from [13], whose range sidelobes are significantly influenced by the modulated data onto its subchirps due to its correlation-based range processing. As for $k_{\Delta} = -0.1$, which corresponds to the maximum tolerable Doppler shift for OFDM [31], [34], the proposed OCDM-based radar and RadCom systems present comparable performance to their OFDM counterpart, while the conventional OCDM-based RadCom system from [13] still yields the worse range sidelobe pattern. Relevant differences in the range profiles obtained with the proposed OCDM-based systems w.r.t. OFDM are only observed for $k_{\Delta} = -0.25$ and $k_{\Delta} = -0.5$, namely, peak splitting and noticeable range-Doppler coupling due to the effects described in (35) and (36). However, it should be noted that these Doppler shift levels yield very high relative radial velocities and are therefore not to be expected in practical scenarios. Additionally, the combination of these Doppler shifts with the range of 30 m ($n_{\Delta} = 200$) leads the proposed OCDM-based radar and sector-modulated OCDM-based RadCom systems into their most critical region in terms of PPLR, PSLR, and ISLR as shown in Fig. 4. The results for these range and Doppler shift pairs are therefore lower bounds on the radar sensing performance of the proposed OCDM-based schemes and better results are expected for less critical combinations of range and Doppler shift values.

To address the FrDM multiplexing strategy for MU or MIMO operation described in Section III-B, similar measurement results to the ones in Fig. 6 are presented in Fig. 7

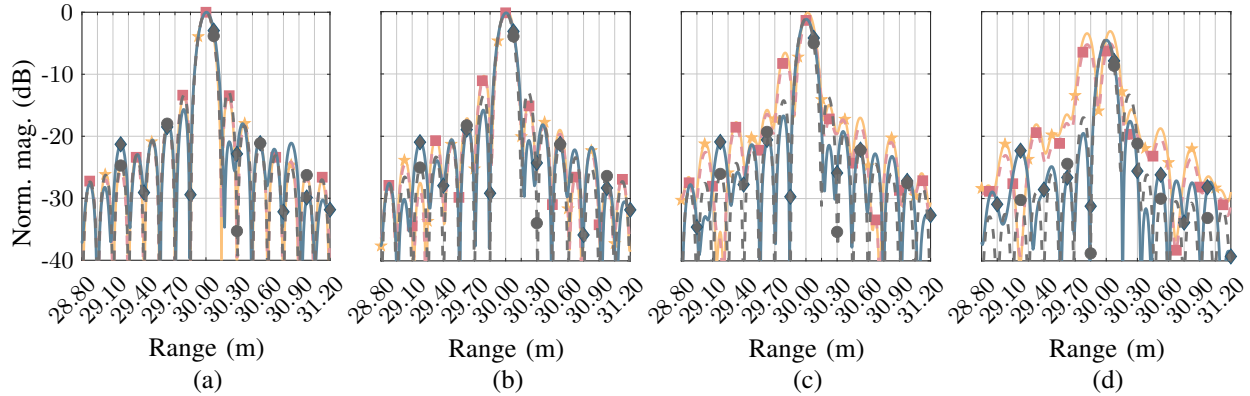


Fig. 6: Range cuts of radar images from measurements with single-input single-output (SISO) OCDM-based radar system (★), sector-modulated OCDM-based RadCom system (■), conventional OCDM-based RadCom system (◆), OFDM-based RadCom system (●) for a single target with relative radial velocity of (a) 0 m/s ($k_{\Delta} = 0$), (b) 92.71 m/s ($k_{\Delta} = -0.1$), (c) 231.78 m/s ($k_{\Delta} = -0.25$), and (d) 463.56 m/s ($k_{\Delta} = -0.5$). In all radar images the actual target range is 30 m ($n_{\Delta} = 200$). Since the three latter modulation schemes yield processing gain around 1 dB lower than the OCDM-based radar system, the magnitudes of the range profiles obtained with each modulation scheme are normalized w.r.t. their respective results at 0 m/s ($k_{\Delta} = 0$) for a fairer comparison.

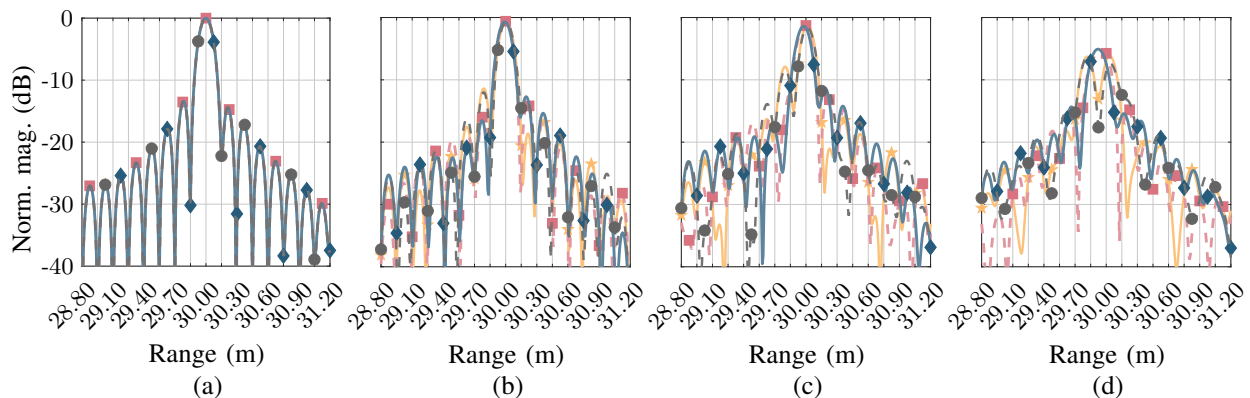


Fig. 7: Range cuts of radar images from measurements with transmit channels $p = 0$ (★), $p = 1$ (■), $p = 2$ (◆), and $p = 3$ (●) in the considered MIMO OCDM-based radar system for a single target with relative radial velocity of (a) 0 m/s ($k_{\Delta} = 0$), (b) 92.71 m/s ($k_{\Delta} = -0.1$), (c) 231.78 m/s ($k_{\Delta} = -0.25$), and (d) 463.56 m/s ($k_{\Delta} = -0.5$). In all radar images the actual target range is 30 m ($n_{\Delta} = 200$).

for signals transmitted by $P = 4$ collocated transmitters and evaluated at a single receiver. For the results in this figure, the same OCDM signal parameters adopted for the SISO OCDM-based radar system as mentioned at the beginning of this section are adopted, leading to the same radar performance parameters listed in Table II. The only exception is the maximum unambiguous range, which is reduced to $R_{\max, \text{ua}}^{\text{MU/MIMO}, P} = 76.8 \text{ m}$ due to the multiplexing among $P = 4$ transmitters. Compared to the results for the SISO OCDM-based radar system in Fig. 6, which are virtually the same as for the transmitter $p = 0$ in the MIMO case, the results from Fig. 7 only differ significantly for $k_{\Delta} = -0.25$ and $k_{\Delta} = -0.5$. This is due to the combined effect of the range-Doppler coupling and Doppler dependent phase terms in (36), which directly influence the peak splitting and range-Doppler coupling effects. As already mentioned previously, however, such high Doppler shift levels are not to be expected in practice.

To assess the communication performance of the proposed OCDM-based RadCom in Section III-C, measurements over a communication channel emulated by re-purposing the previously described RTS were performed with the same SoC

platform from Xilinx, Inc, ensuring time and frequency synchronization between the communication transmitter and receiver with the Schmidl & Cox (S&C) algorithm as described in [35]. For the communication analysis, the proposed sector-modulated OCDM-based RadCom system was compared with the OFDM-based and conventional OCDM-based RadCom systems. Additionally, the same signal parameters adopted for the radar performance analysis were kept for all three modulation schemes, resulting in a data rate of 0.80 Gbit/s for the sector-modulated OCDM-based RadCom system and a data rate of 1.40 Gbit/s for its OFDM and conventional OCDM counterparts, which is influenced by inserted pilot subcarriers in the OFDM case and use of frequency-shift precoding (FSP)-inserted pilots in the conventional OCDM case [36]. The magnitude response of the experienced communication CFR, whose frequency-selectivity is due to the sinc-shaping resulting from the use of an intermediate frequency (IF)-sampling architecture and uncalibrated effects of cables, baluns and filters, is shown in Fig. 8. To enable channel equalization and subsequent extraction of the receive QPSK symbols from the receive signal, the unmodulated subchirp in the sector-modulated OCDM-based RadCom system was used.

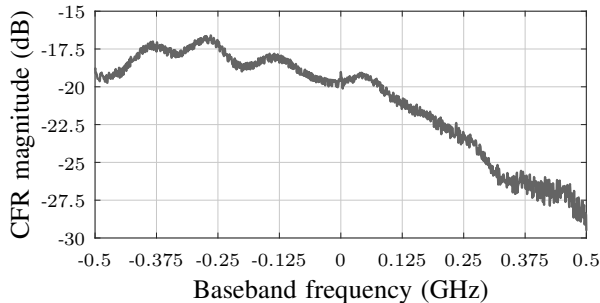


Fig. 8: Magnitude response of the experienced communication CFR.

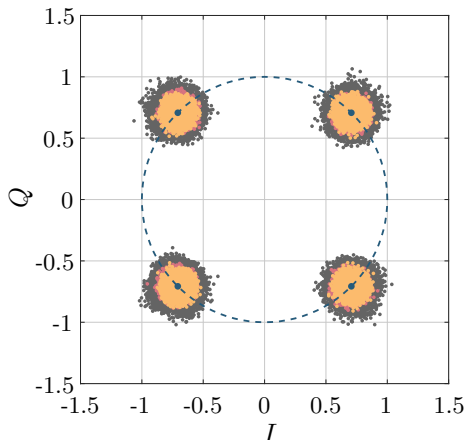


Fig. 9: Normalized receive QPSK constellations: sector-modulated OCDM-based RadCom system (●), conventional OCDM-based RadCom system (●), and OFDM-based RadCom system (●). For reference, an unit-radius circle (---) and a QPSK constellation with unit symbol energy (●) are shown.

As for OFDM- and the conventional OCDM-based RadCom system from [12], channel estimation was performed using the comb-pilot-based techniques, namely the one described in [37] for OFDM and its FSP-based version for the conventional OCDM-based RadCom system [36]. For all three modulation schemes, multiple channel estimates were averaged to reduce noise effect before performing equalization. The obtained normalized receive QPSK constellations are shown in Fig. 9. Based on the achieved results, both sector-modulated and conventional OCDM-based RadCom systems yield virtually the same communication performance. While the first has an estimate SNR of 29.65 dB and an error vector magnitude (EVM) with mean value of -26.27 dB and standard deviation of 5.59 dB, an estimated input SNR of 29.74 dB and EVM with mean value of -26.20 dB and standard deviation of 5.53 dB for the latter. As for the OFDM-based RadCom system, an estimated input SNR of 29.65 dB and EVM with mean value of -27.64 dB and standard deviation of 6.30 dB were obtained. The higher mean and value and lower standard deviation of the EVM in the OCDM-based systems can be explained by the fact that the degradation imposed by channel is spread over all subchirps. Conversely, while a lower EVM mean value is experienced in the OFDM-based RadCom system, its higher standard deviation is due to different subcarriers experiencing different attenuation levels while propagating through the channel. More specifically, the subcarriers on the rightmost side of the spectrum experience

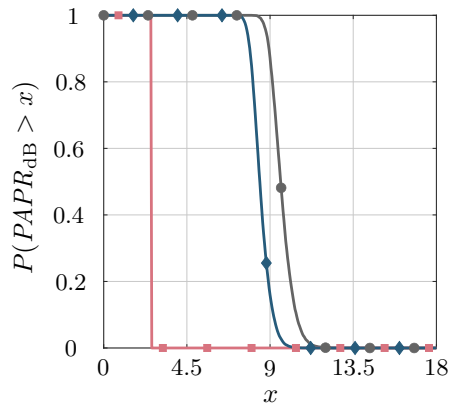


Fig. 10: Simulated baseband PAPR for the considered OCDM-based radar system and its MU/MIMO variant per transmit channel (■), sector-modulated OCDM-based RadCom system (◆) and an OFDM- and conventional OCDM-based RadCom systems (●), all with symbol length of $N = 2048$.

around 10 dB more attenuation than the ones on the leftmost side (see Fig. 8), being therefore more severely degraded and having their receive QPSK symbols shifted away from the reference constellation in Fig. 9. This behavior agrees with the predicted higher robustness of the OCDM-based RadCom systems in frequency-selective channels, e.g., as reported in [3], [9], [15], [38], and leads to a better overall communication performance compared to their OFDM counterpart.

Finally, the simulated complementary cumulative distribution functions (CCDFs) of the baseband PAPR for a single OCDM symbol is shown for the investigated OCDM-based radar system, its MU/MIMO variant, and the proposed sector-modulated OCDM-based RadCom system. For the sake of comparison, the PAPRs of considered OFDM- and conventional OCDM-based RadCom systems in the previous radar and communication analysis are also shown as a baseline. As in [3], the PAPR was calculated assuming an oversampling factor of 20 to capture fast variations of time-domain signals. The particularly low baseband PAPR for the considered OCDM-based radar system and its MU/MIMO variant is explained by the single active subchirp in (25) and (37), which yields a complex exponential signal with a virtually constant envelop in the discrete-time domain after the IDFnT in (1). As for the sector-modulated OCDM-based RadCom system, the presence of active, modulated subchirps in (40) yields nearly 6 dB higher average PAPR. Compared to the OFDM- and conventional OCDM-based RadCom systems, which perform equally, the sector-modulated OCDM-based RadCom system presents reduced PAPR by around 1.1 dB. If lower communication data rates are aimed, this difference can be increased by deactivating some of the QPSK-modulated subchirps, which yields a similar effect to the PAPR reduction by tone reservation in OFDM-based systems.

V. CONCLUSION

This article has investigated the use of discrete-Fresnel domain channel estimation for OCDM-based radar systems. The proposed processing strategy relies on a strategic subchirp allocation for OCDM symbols in the discrete-Fresnel domain and exploits the pulse-compression-like effect of the DFnT.

After a thorough mathematical formulation of the individual and joint effects of time and frequency shifts on OCDM signals in the discrete-Fresnel domain, discrete-Fresnel domain radar channel estimation strategies have been proposed for both SISO and MIMO radar applications, as well as for RadCom operation. Finally, a detailed performance analysis supported by simulation and measurements with a RTS has been carried out assuming a mid-range HAD scenario to validate the contributions of this article and compare the achieved performances with the ones of OFDM- and conventional OCDM-based radar/RadCom systems.

The achieved results have shown that the investigated discrete-Fresnel domain channel estimation for OCDM-based radar and RadCom systems yields comparable performance to OFDM-based radar/RadCom systems in all its forms, i.e., SISO and MIMO operations or sector-modulated RadCom operation. Significant differences, namely peak splitting and range migration, are only observed for Doppler shifts associated with relative radial velocities that are not to be expected in practice. Compared to the conventional OCDM-based RadCom system from a previous work, all of the proposed strategies yield improved radar sensing performance as their range sidelobes are not influenced by modulated data symbols onto subchirps. Additionally, the proposed strategies for SISO and MIMO OCDM-based radar sensing yield significantly lower PAPR than their OFDM and conventional OCDM counterpart. As for the sector-modulated OCDM-based RadCom system, the experienced PAPR reduction is lower, but can be improved in exchange for data rate reduction. For radar-centric systems, where very high data rates are not necessarily a requirement, the proposed sector-modulated OCDM-based RadCom system also appears as an attractive alternative to its OFDM and conventional OCDM counterparts, since it shows robustness for both radar sensing and communication.

APPENDIX

The finite geometric series and its solution used for the derivation of equations in Sections II and III are expressed as

$$\begin{aligned} \sum_{\eta=0}^{\gamma} \alpha^{\eta} &= 1 + \alpha + \alpha^2 + \dots + \alpha^{\gamma} \\ &= \frac{\alpha^{\gamma+1} - 1}{\alpha - 1} \quad \text{for } \alpha \neq 1 \end{aligned} \quad (\text{A.1})$$

for $\eta \in \mathbb{N}$, $\gamma \in \mathbb{N}$, $\alpha \in \mathbb{C}$.

REFERENCES

- [1] B. Schweizer et al., "The fairy tale of simple all-digital radars: How to deal with 100 Gbit/s of a digital millimeter-wave MIMO radar on an FPGA [application notes]," *IEEE Microw. Mag.*, vol. 22, no. 7, pp. 66–76, Jul. 2021.
- [2] C. Vasanelli et al., "Calibration and direction-of-arrival estimation of millimeter-wave radars: A practical introduction," *IEEE Antennas and Propagat. Mag.*, vol. 62, no. 6, pp. 34–45, Dec. 2020.
- [3] L. Giroto de Oliveira, B. Nuss, M. B. Alabd, A. Diewald, M. Pauli, and T. Zwick, "Joint radar-communication systems: Modulation schemes and system design," *IEEE Trans. Microw. Theory Tech.*, vol. 70, no. 3, pp. 1521–1551, Mar. 2022.
- [4] G. Hakobyan and B. Yang, "High-performance automotive radar: A review of signal processing algorithms and modulation schemes," *IEEE Signal Process. Mag.*, vol. 36, no. 5, pp. 32–44, Sept. 2019.
- [5] F. Roos, J. Bechter, C. Knill, B. Schweizer, and C. Waldschmidt, "Radar sensors for autonomous driving: Modulation schemes and interference mitigation," *IEEE Microw. Mag.*, vol. 20, no. 9, pp. 58–72, Sept. 2019.
- [6] C. Waldschmidt, J. Hasch, and W. Menzel, "Automotive radar – from first efforts to future systems," *IEEE J. Microw.*, vol. 1, no. 1, pp. 135–148, 2021.
- [7] L. Giroto de Oliveira et al., "Doppler shift tolerance of accumulation and outer coding in MIMO-PMCW radar," *IEEE Microwave and Wireless Components Letters*, pp. 1–4, Nov. 2021.
- [8] —, "Doppler shift tolerance of typical pseudorandom binary sequences in PMCW radar," *Sensors*, vol. 22, no. 9, pp. 1–21, Apr. 2022.
- [9] X. Ouyang and J. Zhao, "Orthogonal chirp division multiplexing," *IEEE Trans. Commun.*, vol. 64, no. 9, pp. 3946–3957, 2016.
- [10] Q. Wang, A. Kakkavas, X. Gong, and R. A. Stirling-Gallacher, "Towards integrated sensing and communications for 6G," Feb. 2021.
- [11] F. Liu, Y. Cui, C. Masouros, J. Xu, T. X. Han, Y. C. Eldar, and S. Buzzi, "Integrated sensing and communications: Towards dual-functional wireless networks for 6G and beyond," *IEEE J. Sel. Areas Commun. (Early Access)*, pp. 1–1, 2022.
- [12] L. Giroto de Oliveira, M. B. Alabd, B. Nuss, and T. Zwick, "An OCDM radar-communication system," in *2020 14th European Conf. Antennas Propag.*, Mar. 2020, pp. 1–5.
- [13] L. Giroto de Oliveira, B. Nuss, M. B. Alabd, Y. Li, L. Yu, and T. Zwick, "MIMO-OCDM-based joint radar sensing and communication," in *2021 15th European Conf. Antennas Propag.*, Mar. 2021, pp. 1–5.
- [14] Y. Wang, Z. Shi, X. Ma, and L. Liu, "A joint sonar-communication system based on multicarrier waveforms," *IEEE Signal Process. Lett.*, vol. 29, pp. 777–781, 2022.
- [15] M. S. Omar and X. Ma, "Performance analysis of OCDM for wireless communications," *IEEE Trans. Wireless Commun.*, vol. 20, no. 7, pp. 4032–4043, Jul. 2021.
- [16] X. Ouyang, C. Antony, F. Gunning, H. Zhang, and Y. L. Guan, "Discrete Fresnel transform and its circular convolution," *CoRR*, vol. abs/1510.00574, 2015. [Online]. Available: <http://arxiv.org/abs/1510.00574>
- [17] X. Ouyang, O. A. Dobre, Y. L. Guan, and J. Zhao, "Chirp spread spectrum toward the Nyquist signaling rate – orthogonality condition and applications," *IEEE Signal Process. Lett.*, vol. 24, no. 10, pp. 1488–1492, 2017.
- [18] R. Bomfin, M. Chafii, and G. Fettweis, "Low-complexity iterative receiver for orthogonal chirp division multiplexing," in *2019 IEEE Wireless Commun. and Netw. Conf. Workshop*, Apr. 2019, pp. 1–6.
- [19] M. S. Omar and X. Ma, "The effects of narrowband interference on OCDM," in *2020 IEEE 21st Inter. Workshop Signal Process. Advances in Wireless Commun.*, May 2020, pp. 1–5.
- [20] S. Bhattacharjee, K. V. Mishra, R. Annavajjala, and C. R. Murthy, "An overview of signal processing techniques for joint communication and radar sensing," Nov. 2021.
- [21] X. Ouyang, O. A. Dobre, and J. Zhao, "Unbiased channel estimation based on the discrete fresnel transform for CO-OFDM systems," *IEEE Photonics Technol. Lett.*, vol. 29, no. 8, pp. 691–694, 2017.
- [22] X. Ouyang, C. Antony, G. Talli, and P. D. Townsend, "Robust channel estimation for coherent optical orthogonal chirp-division multiplexing with pulse compression and noise rejection," *Journal Lightw. Technol.*, vol. 36, no. 23, pp. 5600–5610, 2018.
- [23] R. Zhang, Y. Wang, and X. Ma, "Channel estimation for OCDM transmissions with carrier frequency offset," *IEEE Wireless Commun. Lett.*, vol. 11, no. 3, pp. 483–487, Mar. 2022.
- [24] L. Giroto de Oliveira, M. de Lima Filomeno, H. V. Poor, and M. V. Ribeiro, "Orthogonal chirp-division multiplexing for power line sensing via time-domain reflectometry," *IEEE Sensors J.*, vol. 21, no. 2, pp. 955–964, 2021.
- [25] L. de M. B. A. Dib, G. R. Colen, M. de L. Filomeno, and M. V. Ribeiro, "Orthogonal chirp division multiplexing for baseband data communication systems," *IEEE Syst. J.*, vol. 14, no. 2, pp. 2164–2174, 2020.
- [26] T. M. Schmidl and D. C. Cox, "Robust frequency and timing synchronization for OFDM," *IEEE Trans. Commun.*, vol. 45, no. 12, pp. 1613–1621, Dec. 1997.
- [27] X. Ouyang, "Digital signal processing for fiber-optic communication systems," Ph.D. dissertation, University College Cork, Ireland, 2017.
- [28] T. Hwang, C. Yang, G. Wu, S. Li, and G. Ye Li, "OFDM and its wireless applications: A survey," *IEEE Trans. on Veh. Technol.*, vol. 58, no. 4, pp. 1673–1694, Aug. 2009.
- [29] V. Winkler, "Range doppler detection for automotive FMCW radars," in *2007 European Microw. Conf.*, Oct. 2007, pp. 1445–1448.

- [30] B. Nuss, "Frequenzkamm-basiertes breitbandiges MIMO-OFDM-Radar," Ph.D. dissertation, Inst. Radio Freq. Eng. Electron., Karlsruhe Inst. Technol., Germany, 2021, (in German).
- [31] B. Nuss, J. Mayer, and T. Zwick, "Limitations of MIMO and multi-user access for OFDM radar in automotive applications," in *2018 IEEE MTT-S Int. Conf. Microw. Intell. Mobility*, Apr. 2018, pp. 1–4.
- [32] G. Lellouch, A. K. Mishra, and M. Inggs, "Design of OFDM radar pulses using genetic algorithm based techniques," *IEEE Trans. Aerosp. Electron. Syst.*, vol. 52, no. 4, pp. 1953–1966, 2016.
- [33] A. Diewald, C. Kurz, P. V. Kannan, M. Giessler, M. Pauli, B. Göttel, T. Kayser, F. Gauterin, and T. Zwick, "Radar target simulation for vehicle-in-the-loop testing," *Vehicles*, vol. 3, no. 2, pp. 257–271, 2021.
- [34] C. Sturm and W. Wiesbeck, "Waveform design and signal processing aspects for fusion of wireless communications and radar sensing," *Proc. IEEE*, vol. 99, no. 7, pp. 1236–1259, Jul. 2011.
- [35] M. de L. Filomeno et al., "Joint channel estimation and Schmidl & Cox synchronization for OCDM-based systems," *IEEE Commun. Lett. (Early Access)*, pp. 1–5, May 2022.
- [36] M. S. Omar and X. Ma, "Pilot symbol aided channel estimation for OCDM transmissions," *IEEE Commun. Lett.*, vol. 26, no. 1, pp. 163–166, 2022.
- [37] Y. L. Sit, B. Nuss, and T. Zwick, "On mutual interference cancellation in a MIMO OFDM multiuser radar-communication network," *IEEE Trans. Veh. Technol.*, vol. 67, no. 4, pp. 3339–3348, Dec. 2018.
- [38] T. F. Moreira, A. Camponogara, S. Baig, and M. V. Ribeiro, "Data rate and bit error probability in narrowband PLC systems: OCDM versus HS-OFDM," in *39th Brazilian Symp. Telecommun. Signal Process.*, Sep. 2021, pp. 1–5.



Lucas Giroto de Oliveira (Graduate Student Member, IEEE) received the B.Sc. and M.Sc. degrees in electrical engineering with a major in electronic systems from the Federal University of Juiz de Fora (UFJF), Juiz de Fora, Brazil, in 2017 and 2019, respectively. He is currently pursuing the Dr.-Ing. (Ph.D.E.E.) degree at the Karlsruhe Institute of Technology (KIT), Karlsruhe, Germany.

He was with the Laboratório de Comunicações (LCom), UFJF, from June 2014 to March 2019. From April 2015 to March 2016, he was also with

the Digital Communications Group, University of Duisburg-Essen, Duisburg, Germany. Since April 2019, he has been with the Institute of Radio Frequency Engineering and Electronics (IHE), KIT, where he is currently a Research Associate. His research interests are in the areas of signal processing, digital communication, and their applications to integrated radar sensing and communication systems and networks.

Mr. Giroto de Oliveira was a recipient of the Science without Borders (CsF) scholarship funded by Coordenação de Aperfeiçoamento de Pessoal de Nível Superior (CAPES), Brazil, from September 2014 to March 2016, and of the Research Grant for Doctoral Programmes in Germany from the German Academic Exchange Service (DAAD), Germany, from April 2019 to March 2021. He was also a co-author of the Best Conference Paper award winning paper at the 2022 International Workshop on Antenna Technology (iWAT).



Benjamin Nuss (Graduate Student Member, IEEE) received the B.Sc. and M.Sc. degrees in electrical engineering and information technology from the Karlsruhe Institute of Technology (KIT), Karlsruhe, Germany, in 2012 and 2015, respectively, and the Dr.-Ing. (Ph.D.E.E.) degree from KIT, in 2021.

He is currently working as a Group Leader for radar systems at the Institute of Radio Frequency Engineering and Electronics (IHE). The focus of his work is on the development of efficient future radar waveforms and interference mitigation techniques

for multi-user scenarios. His current research interests include orthogonal frequency-division multiplexing-based multiple-input multiple-output radar systems for future automotive applications and drone detection. He was also the author and co-author of the best publication of 2021 and 2022 within the ITG Society, which was awarded the VDE ITG Prize.



Mohamad Basim Alabd (Graduate Student Member, IEEE) received the B.Sc. and M.Sc. degrees in electronics and telecommunications from Al-Baath University, Homs, Syria, in 2010 and 2014, respectively.

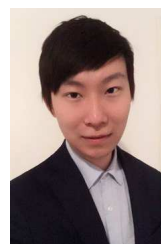
He was a Research Associate with the Chair of Information Systems, Innovation & Value Creation (WI1), Friedrich-Alexander-Universität Erlangen-Nürnberg, Nuremberg, Germany. From 2010 to 2014, he was with Syrian Telecommunication Company, Homs, and worked there in different positions.

He has been a Research Associate with the Institute of Radio Frequency Engineering and Electronics (IHE), Karlsruhe Institute of Technology, Karlsruhe, Germany, since 2017. His current research interests include chirp sequence (CS) joint radar-communication and orthogonal frequency-division multiplexing-based multiple-input multiple-output radar systems for future automotive applications.



Axel Diewald (Graduate Student Member, IEEE) received the B.Sc. and M.Sc. degrees in electrical engineering and information technology from the Karlsruhe Institute of Technology (KIT), Karlsruhe, Germany, in 2015 and 2017, respectively, where he is currently pursuing the Ph.D. degree in electrical engineering (EE) at the Institute of Radio Frequency Engineering and Electronics (IHE).

His main research interests include digital radar target simulation for the purpose of automotive radar sensor validation and realistic target modeling.



Yueheng Li (Graduate Student Member, IEEE) received his B.Sc. in telecommunication science and technology from Shandong University, Jinan, China in 2014. In 2018, he further received his M.Sc. in communication and information technology from University of Bremen, Bremen, Germany. Since 2018, he has been a scientific employee and working toward the Dr.-Ing. (Ph.D.E.E.) degree at the Institute of Radio Frequency Engineering and Electronics (IHE), Karlsruhe, Germany. His research focuses on mobile wireless communication systems using

programmable metasurface.



Linda Gehre received the B.Sc. degree in electrical engineering and information technology from the Karlsruhe Institute of Technology (KIT), Karlsruhe, Germany, in 2021, where she is pursuing the M.Sc. degree and working as a student assistant at the Institute of Radio Frequency Engineering and Electronics (IHE). Her research interests are in the field of radar sensing and communication systems.



Xueyun Long received the B.Sc. degree in electronic information engineering from the Beijing Institute of Technology, Beijing, China, in 2018, the M.Sc. degree in electronic and information technology, in 2021, from the Karlsruhe Institut of Technology, Karlsruhe, Germany, where she is currently working toward the Dr.-Ing. (Ph.D.E.E) degree in electrical engineering with the Institute of Radio Frequency Engineering and Electronics, Karlsruhe, Germany. Her research interests include exposure and programmable metasurface.



Theresa Antes received the B.Sc. and M.Sc. degrees in electrical engineering and information technology from the Karlsruhe Institute of Technology (KIT), Karlsruhe, Germany, in 2018 and 2020, respectively, where she is currently pursuing the Ph.D. degree in electrical engineering (EE) at the Institute of Radio Frequency Engineering and Electronics (IHE). Her main research interests include signal processing, high-accuracy radar systems, and radar-based gesture recognition.



Johannes Galinsky received the B.Sc. and M.Sc. degrees in electrical engineering and information technology from the Karlsruhe Institute of Technology (KIT), Karlsruhe, Germany, in 2019 and 2022, respectively, where he is currently pursuing the Ph.D. degree in electrical engineering (EE) at the Institute of Radio Frequency Engineering and Electronics (IHE). His main research interests include signal processing, digital radar and joint communication & sensing.



Thomas Zwick (Fellow, IEEE) received the Dipl.-Ing. (M.S.E.E.) and Dr.-Ing. (Ph.D.E.E.) degrees from the Universität Karlsruhe (TH), Karlsruhe, Germany, in 1994 and 1999, respectively.

From 1994 to 2001, he was a Research Assistant with the Institut für Höchstfrequenztechnik und Elektronik (IHE), TH. In February 2001, he joined IBM as Research Staff Member at the IBM Thomas J. Watson Research Center, Yorktown Heights, NY, USA. From October 2004 to September 2007, he was with Siemens AG, Lindau, Germany. During that period, he managed the RF development team for automotive radars. In October 2007, he became a Full Professor with the Karlsruhe Institute of Technology (KIT), Karlsruhe. He is currently the Director of the Institute of Radio Frequency Engineering and Electronics (IHE), KIT. He is a co-editor of three books and the author or a co-author of 120 journal articles, over 400 contributions at international conferences, and 15 granted patents. His research topics include wave propagation, stochastic channel modeling, channel measurement techniques, material measurements, microwave techniques, millimeter-wave antenna design, wireless communication, and radar system design.

Dr. Zwick has been a member of the Heidelberg Academy of Sciences and Humanities since 2017. Since 2019, he has been a member of acadtech (German National Academy of Science and Engineering). His research team received over ten best paper awards at international conferences. In 2013, he was the General Chair of the International Workshop on Antenna Technology (iWAT 2013) in Karlsruhe and the IEEE MTT-S International Conference on Microwaves for Intelligent Mobility (ICMIM) in Heidelberg in 2015. He was the TPC Chair of the European Microwave Conference (EuMC) 2013 and the General TPC Chair of the European Microwave Week (EuMW) 2017. In 2023, he will be the General Chair of EuMW in Berlin. He has served on the technical program committees (TPC) of several scientific conferences. From 2008 to 2015, he was the president of the Institute for Microwaves and Antennas (IMA). He was selected as a Distinguished IEEE Microwave Lecturer for the 2013-2015 period with his lecture on "QFN Based Packaging Concepts for Millimeter-Wave Transceivers." In 2019, he became the Editor-in-Chief of the IEEE MICROWAVE AND WIRELESS COMPONENTS LETTERS. In 2022 he was awarded an honorary doctorate of the Faculty of Electrical Engineering and Informatics at the Budapest University of Technology and Economics in Hungary.